Variability in the El Niño–Southern Oscillation Through a Glacial-Interglacial Cycle

Alexander W. Tudhope,[1,2]* Colin P. Chilcott,[1] Malcolm T. McCulloch,[3] Edward R. Cook,[4] John Chappell,[3] Robert M. Ellam,[5] David W. Lea,[6] Janice M. Lough,[2] Graham B. Shimmield[7]

The El Niño–Southern Oscillation (ENSO) is the most potent source of interannual climate variability. Uncertainty surrounding the impact of greenhouse warming on ENSO strength and frequency has stimulated efforts to develop a better understanding of the sensitivity of ENSO to climate change. Here we use annually banded corals from Papua New Guinea to show that ENSO has existed for the past 130,000 years, operating even during "glacial" times of substantially reduced regional and global temperature and changed solar forcing. However, we also find that during the 20th century ENSO has been strong compared with ENSO of previous cool (glacial) and warm (interglacial) times. The observed pattern of change in amplitude may be due to the combined effects of ENSO dampening during cool glacial conditions and ENSO forcing by precessional orbital variations.

Coupled ocean-atmosphere interactions rooted in the tropical Pacific Ocean play a crucial role in modulating global climate on interannual (*1*–*4*), decadal (*5*–*7*), and, arguably, glacial-interglacial (10^5 year) (*8*, *9*) time scales. Best known in this context is the ENSO (*10*), which has a variable period ranging from 2.5 to 7 years, but usually focused in the 3- to 5-year band. ENSO has gained notoriety over the past two decades due to the unusually strong El Niño ("warm") events of 1982/83 and 1997/98, both of which had widespread ecological, social, and economic impacts. Despite recent advances in our understanding of the physics behind the ENSO phenomenon (*11*), key aspects of the system remain poorly understood. These include the nature and origin of variability in the strength and frequency of ENSO and the sensitivity of the ENSO system to changes in climatic boundary conditions. This variability, forced and unforced, is crucial to determining the predictability and global impacts of ENSO, now and in a greenhouse-warmed future (*12*–*15*). One of the major obstacles to progress in this field has been the lack of instrumental and high-resolution proxy records of sufficient length to reveal the range of natural variability in ENSO and its response to global climate change.

Here we use geochemical analyses of annually banded massive *Porites* corals from Papua New Guinea to investigate variability in ENSO at intervals through the last glacial-interglacial cycle of Earth history. As they grow, reef-building corals record climatic information in the chemistry of their aragonitic skeletons. Retrospective analysis of cores collected from large living coral colonies has been shown to be a particularly powerful tool for reconstructing sea surface temperature (SST) and salinity (rainfall) variations associated with ENSO (*16*, *17*). Due to the presence of annual bands in skeletal composition and structure, rapid growth rates (8 to 20 mm/year), and longevity of coral colonies, these coral climate-proxy records can have a temporal resolution of about a month over several hundred years. The same species of massive corals are also well preserved in some late Quaternary exposed reef sequences, from which they may be sampled and accurately dated by U-series techniques. This suite of attributes, allowing annually resolved records to be constructed, makes tropical corals possibly unique in their potential to reveal the nature and evolution of ENSO dynamics on 10^3 to 10^5 year time scales.

The record of modern ENSO in corals from Papua New Guinea. The north coast of Papua New Guinea lies in the heart of the western equatorial Pacific Warm Pool, an area of exceptionally warm surface ocean, strong atmospheric convection, and high rainfall that plays a pivotal role in ENSO dynamics (Fig. 1). The climate of the region is fundamentally linked to ENSO variability, with relative drought and slightly reduced SSTs characterizing the El Niño phase. These climatic variations are recorded in the skeletal geochemistry of corals living along the coast (*18*).

In this study, we use the oxygen isotopic ($\delta^{18}O$) composition of the coralline aragonite to reconstruct past ENSO activity. This tracer responds to water temperature through a temperature-dependent fractionation [~ -0.2‰ $\delta^{18}O$/°C (*19*, *20*)], as well as to changes in rainfall, due to the influence of isotopically light (more negative $\delta^{18}O$) rainfall on surface ocean composition. Because SST and rainfall are intimately linked in tropical areas of strong convective rainfall such as the western equatorial Pacific, the two factors combine to produce an enhanced climatic signal in coral skeletal $\delta^{18}O$. That is, the wet and warm conditions during the La Niña phase of the Southern Oscillation result in deposition of isotopically light coral skeleton, whereas the dry and cool conditions during the El Niño phase result in isotopically heavy skeletal oxygen (Fig. 2A) (*18*).

The approach taken in this study is to

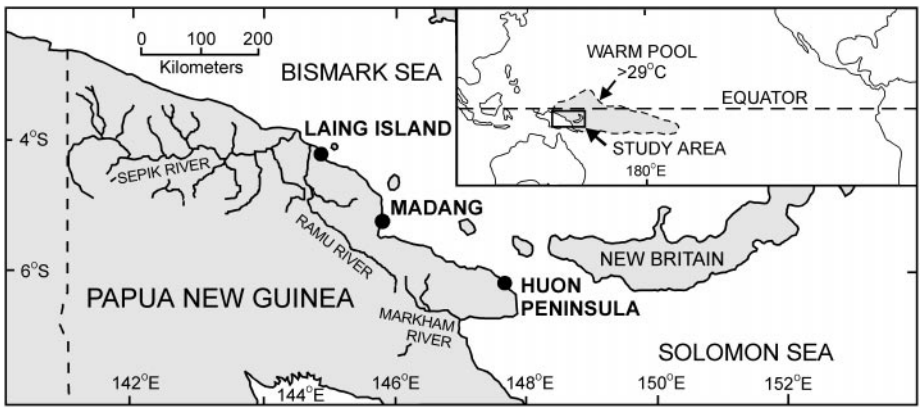

Fig. 1. Location of study sites.

[1]Department of Geology & Geophysics, Edinburgh University, Edinburgh, EH9 3JW, UK. [2]Australian Institute of Marine Science, Townsville, Queensland 4810, Australia. [3]Research School of Earth Sciences, Australian National University, Canberra, ACT 0200, Australia. [4]Tree-Ring Laboratory, Lamont-Doherty Earth Observatory, New York 10964, USA. [5]Scottish Universities Environmental Research Centre, East Kilbride, Glasgow G75 0QF, UK. [6]Department of Geological Sciences and Marine Science Institute, University of California, Santa Barbara, CA 93106, USA. [7]Dunstaffnage Marine Laboratory, Oban, Argyll, PA34 4AD, UK.

*To whom correspondence should be addressed. E-mail: sandy.tudhope@ed.ac.uk

analyze cores collected from fossil corals to produce high-resolution, multidecadal windows of past climate and to infer from these the status of ENSO variability. To validate this approach, it is important first to demonstrate the regional reproducibility of coral $\delta^{18}O$ records from the study area and their reliability as ENSO proxies. It is also necessary to produce benchmark "modern ENSO" coral records against which fossil coral data may be compared. To this end, we analyzed modern *Porites* corals from three locations (Huon Peninsula, Madang, and Laing Island) separated by up to 380 km (Fig. 1) and compared the resulting geochemical records with local and regional climatic indices.

Cores from the living corals were subsampled into 1- or 2-mm growth increments to yield 6 to 14 samples per year, which were then analyzed for $\delta^{18}O$ and $\delta^{13}C$ (*21*). The chronologies were subsequently developed on the basis of seasonality in skeletal $\delta^{18}O$ and $\delta^{13}C$, supported by examination of annual skeletal density and fluorescent banding. To facilitate examination of the ENSO component of variability, we bandpass-filtered the coral and instrumental records to isolate the 2.5- to 7-year band (*22*). The resulting time series (Fig. 3) are all strongly correlated and clearly display the well-known pattern of ENSO variability since 1880. These results confirm that the Papua New Guinea coral $\delta^{18}O$ records are robust proxies for ENSO timing, frequency, and amplitude, and they provide the required benchmark for our paleo-ENSO studies.

Fossil corals in Papua New Guinea. Parts of the north coast of Papua New Guinea are undergoing tectonic uplift due to rapid convergence of the West Pacific and Australian plates. This has resulted in spectacular subaerial exposures of late Quaternary coral reefs. Most of the fossil corals for this study were collected from the well-characterized raised reef terraces on the Huon Peninsula, where long-term uplift rates range from 1 to 4 m per thousand years (ky) (*23*). These terraces include reefs that grew during previous glacial times of low global sea level, as well as reefs that grew during previous interglacial times. This situation makes it possible to sample corals which grew during periods when climatic boundary conditions were substantially different to those of today.

For this study, we collected cores from in situ fossil massive *Porites* corals exposed in cliffs representing several phases of reef growth over the last glacial-interglacial cycle

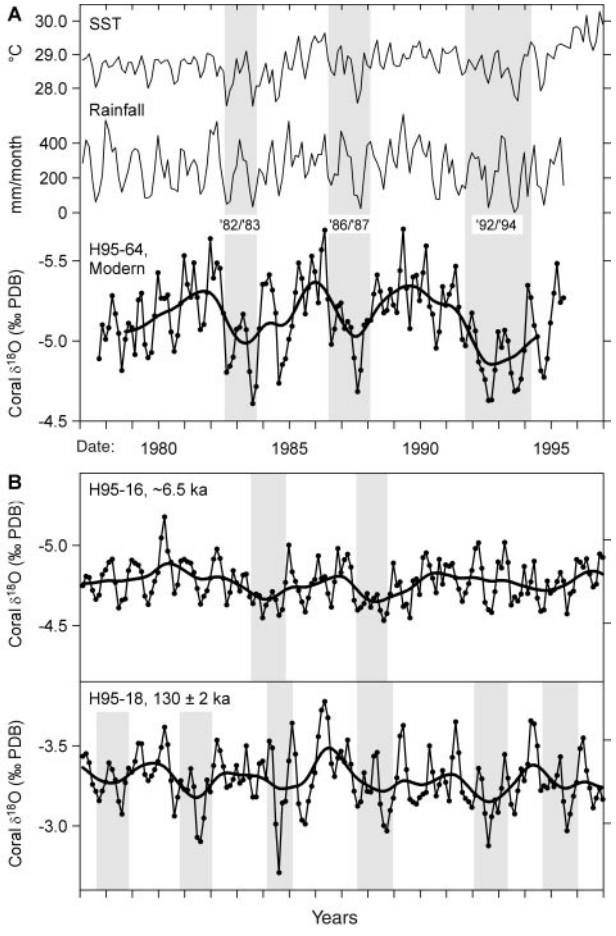

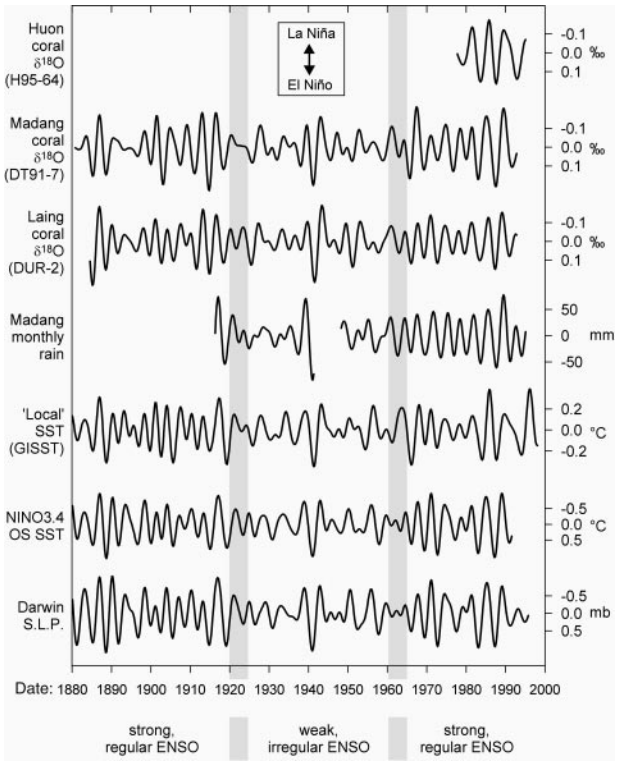

Fig. 2 (left). (**A**) Comparison of coral skeletal $\delta^{18}O$, rainfall and SST time series. The rainfall record is from Madang, the SST record is the IGOSS nmc blended ship and satellite data (*58*) for the 1° square centered on 147.5°E, 6.5°S, and coral H95-64 is from the Huon Peninsula (Fig. 1). All records are interpolated to a resolution of eight samples per year (thin lines). In addition, the coral record has been smoothed with a binomial filter (thick line) to remove seasonality. Historical El Niño events are shown by shading. The double peak in wet/warm season (i.e., more negative $\delta^{18}O$) values seen in some years in the coral record reflects the distinct double peak in wet season rainfall caused by the passage of the Inter-Tropical Convergence Zone southward over the area at the start of the wet season then back northward at the end of the wet season. (**B**) Fossil coral skeletal $\delta^{18}O$ time series for comparison with the modern records. Inferred paleo–El Niño events are shown by shading. Coral H95-16 has the weakest ENSO signal of all the fossil corals sampled. Although close to the sampling and analytical resolution of these records, double peaks in wet/warm season values in some years are suggestive of similar seasonal development to that of the modern era and imply excellent preservation of the proxy climate signal. **Fig. 3 (right).** ENSO variability since 1880. Modern coral skeletal $\delta^{18}O$ and instrumental climate records have been filtered with a Gaussian bandpass filter (*53*) to reveal the 2.5- to 7-year (ENSO) components of variability. For all parameters, the polarity of the *y* axis has been set so that the El Niño phase of the Southern Oscillation would be expected to result in a downward anomaly in the curve. The "local" SST record is the reconstruction for the 1° square centered on 146.5°E, 5.5°S from the GISST2.3b data set of the UK Meteorological Office (*59*); the NINO3.4 OS SST is the optimally smoothed SST reconstruction for the NINO3.4 region in the equatorial central-western Pacific (*60*). Darwin sea level pressure and NINO3.4 SST are widely recognized indices of ENSO activity. The pattern of relatively weak and irregular ENSO activity in the middle of the 20th century (but with a major event in the early 1940s) is a well-known feature of historical ENSO variability.

of Earth history. Reefs that grew during the last glacial maximum (LGM), about 20,000 years ago (20 ka) when global sea level was ~120 m lower than today, are still below present-day sea level (*24*). However, to ensure that we sampled reefs that grew during times of global coolness and large high-latitude ice sheets, we collected cores from corals that grew when global sea level was 70 to 100 m lower than today, around 40 ka, and during the penultimate deglaciation around 130 ka.

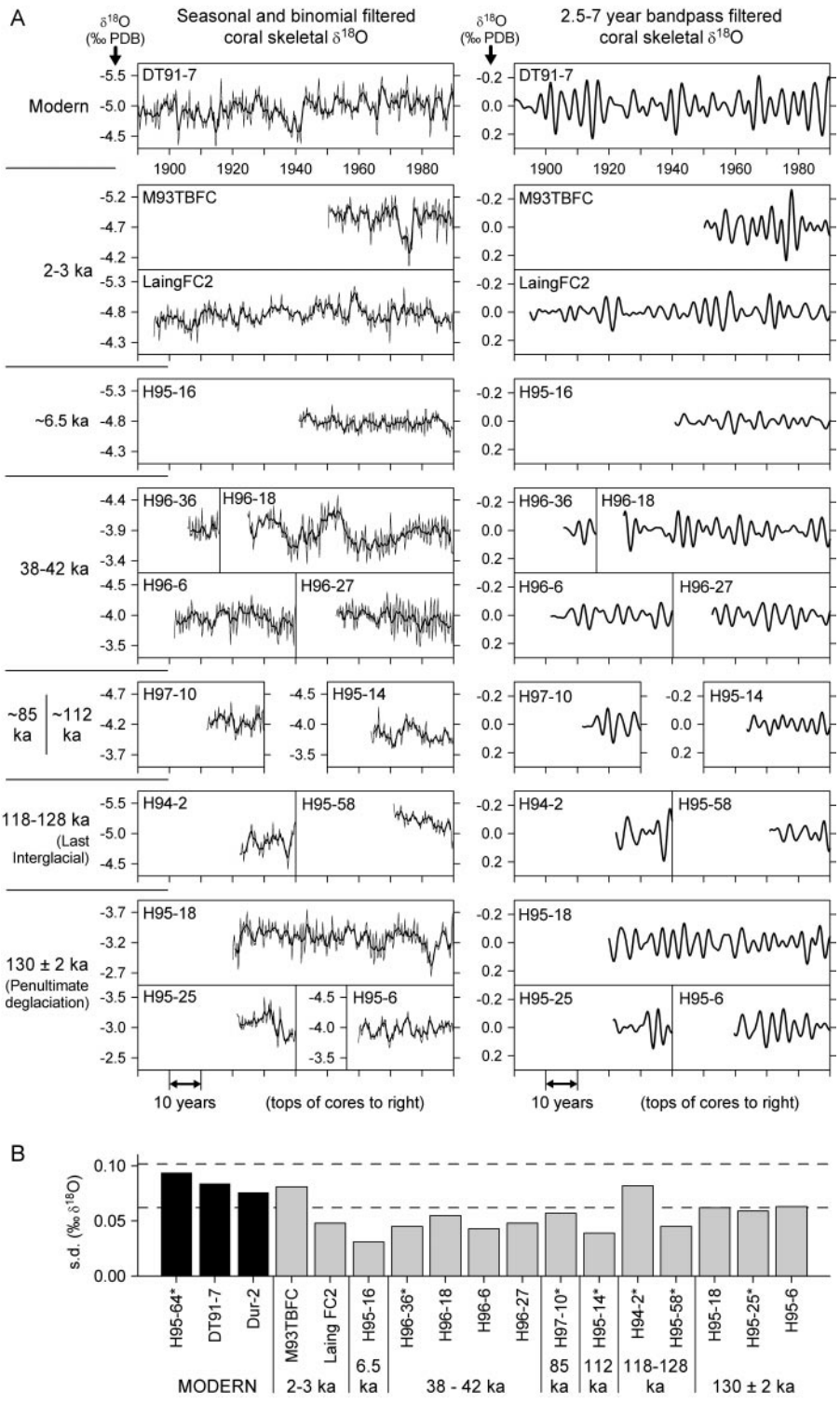

Fig. 4. Paleo-ENSO variability from fossil corals. (**A**) (Left) Seasonal resolution (thin lines) and 2.25-year binomial-filtered (thick lines) skeletal $\delta^{18}O$ records from all fossil corals used in this study, with the record from modern coral DT91-7 shown for comparison. (Right) 2.5- to 7-year (ENSO) bandpass-filtered coral $\delta^{18}O$ time series. (**B**) Standard deviation of the 2.5- to 7-year (ENSO) bandpass-filtered time series of all modern and fossil corals discussed in this study. Asterisk indicates that the time series is <30 years long. The horizontal dashed lines indicate maximum and minimum values of standard deviation for sliding 30-year increments in the modern coral records. Black bars, modern corals; gray bars, fossil corals.

Corals that are subaerially exposed for long periods of time ($>10^3$ years) are prone to diagenetic alteration that may compromise their utility for geochemically based paleoclimatic reconstruction (*25*). Therefore, as an initial check on the quality of our sampled material, we screened the fossil cores geochemically and petrographically (*26*). Fourteen multidecadal cores that passed this quality control were subsampled, analyzed for $\delta^{18}O$ and $\delta^{13}C$, and provided with an annual chronology with the same techniques used for the living corals. The ages of the corals were determined by $^{230}Th/^{234}U$ dating (*27*), supported by knowledge of their stratigraphic position within previously dated sections (Table 1) [Web table 1 (*28*)].

ENSO variability in records from fossil corals. The skeletal $\delta^{18}O$ time series generated from the fossil corals all display well-preserved seasonality (Figs. 2B and 4). In addition, all of the fossil coral records display some, but variable, concentrations of variance in the typical ENSO frequency band. Examination of the relation between the interannual variations and the structure of the seasonal cycle in the fossil corals reveals a pattern that is very similar to that seen in the ENSO cycle in modern corals. That is, more positive interannual excursions in coralline $\delta^{18}O$ (interpreted as cool and dry conditions during the El Niño phase) are generally a reflection of isotopically more positive (cool and dry) anomalies in both the wet and dry season values over a 12- to 18-month period (Fig. 2). This supports the view that the interannual variations seen in the fossil records are indeed a reflection of a paleo-ENSO system.

The fossil coral records come from seven distinct time periods. Four of these are times of substantially lower global sea level during high latitude glaciation (38 to 42 ka, ~85 ka, ~112 ka, and during the penultimate deglaciation 130 ± 2 ka), whereas the other three periods are representative of high sea-level interglacial conditions. Corals within each group are of similar, but probably not overlapping age. Therefore, by grouping corals of similar age, we are effectively increasing the number of observations (number of years) for these time periods. We note that corals from the same time period tend to have similar total variance (Fig. 4). This is especially true for the four corals from 38 to 42 ka, and the three corals from 130 ± 2 ka, suggesting that, for these times at least, the coral records are probably giving a representative view of "average" ENSO variability over longer (e.g., 10^3 year) time scales. This is an important observation, because we have no good a pri-

ori knowledge of the nature and magnitude of changes in ENSO variability on centennial to millennial time scales.

Because the modern ENSO is a broad-band and nonstationary feature in the frequency domain (i.e., its periodicity ranges from 2.5 to 7 years) and because our fossil records are short, we have limited ability to detect any subtle changes in dominant ENSO frequency through time. However, on the basis of inspection of the filtered and unfiltered time series (Fig. 4) and supported by results (*29*) of spectral analysis, we see no evidence for any major change in ENSO frequency or regularity.

One of the striking features of the results is that variance in the ENSO band is greater in the modern coral records than it is in 12 of 14 of the fossil corals (Fig. 4). The two exceptions (which have ENSO variance similar to the modern corals) are a short (18-year) record (H94-2) from the last interglacial and the late Holocene M93TBFC time series that contains an exceptional (~6-year duration) El Niño–like event, which has increased the total variance of the 40-year-long record. Therefore, we have no evidence from fossil corals of sustained ENSO activity equal to or greater than that which occurred over the past 120 years. ENSO variance is lowest in the records from ~6.5 and ~112 ka and at intermediate levels for all other periods. Although total variance in the 2.5- to 7-year band provides one measure of ENSO strength, a potentially more sensitive discriminator between ENSO activity of different periods may be the occurrence of "extreme" high-amplitude events. Corals from the modern, 2 to 3 ka and last interglacial periods contain the highest amplitude events, whereas the ~6.5 and ~112 ka corals show the least tendency for extreme events (Fig. 5A) [Web fig. 1 (*28*)]. Therefore, high total variance is usually accompanied by, and is at least partially a function of, the occurrence of high-amplitude events.

Our results suggest that ENSO has been a persistent component of the climate system over the past 130 ka but that there have been substantial changes in its strength through time. It is difficult to assess rigorously the statistical significance of these apparent differences in ENSO strength due to the relative shortness of the continuous records. However, as an initial step, we used the nonparametric Conover test for equal variances (*30*) to assess the significance of differences in total variance in the 2.5- to 7-year ENSO band between the eight time periods (including the modern) represented by our corals (*31*). Although the shortness of the pooled data in some of the time periods means that these results must be interpreted with caution, we find evidence for some statistically significant ($P < 0.01$) differences in ENSO variance [Web table 2 (*28*)]. In particular, the amplitude of ENSO during the modern period appears to have been significantly greater than during most other periods, and ENSO at 6.5 ka was significantly less vigorous than during most other times.

Before discussing the broader climatic implications of these results, it is important to assess the possibility that some factor other than ENSO variability has contributed to the different interannual variances shown by the fossil corals. Diagenetic alteration is a candidate. However, the fact that even subtle details of the annual cycle in skeletal $\delta^{18}O$ are preserved in our fossil corals (Fig. 2) argues strongly against any significant diagenetic overprint on the coralline $\delta^{18}O$ record. Therefore, we believe that the interannual isotopic signal is a primary, climatic one. Furthermore, because our records come from a region at the centre of ENSO dynamics, our proxy does not depend on potentially tenuous teleconnections, and, consequently, is likely to be robust.

Changes in mean climate in the western equatorial Pacific. It is pertinent to consider how mean climate conditions might have changed over the periods represented by our coral records. Proxy evidence from analysis of deep sea sediment cores now suggests that the surface equatorial Pacific was probably ~3°C cooler at the LGM (~20 ka), 2° to 3°C cooler throughout much of the interval from 70 to 30 ka and similar to or slightly warmer than present during the last interglacial (~118 to 128 ka) (*32*). In addition, during glacial times the mean zonal SST gradient was probably slightly stronger than present,

Table 1. Location, age, paleo-sea level, and paleo-SST for fossil corals. Roman numerals relate to previously described Huon Peninsula raised reefs (*23*, *62*). Ages reported here are $^{230}Th/^{234}U$ ages. Values in bold indicate direct ^{230}Th age determinations from the corals that are in good agreement with the previously dated ($\pm 2\sigma$, or the mean of ages if more than one determination was made from a single coral; $\pm 2\sigma$); other ages are based on location within previously dated stratigraphy (*40*, *62*–*64*). See Web table 1 (*28*) for full details of ^{230}Th age determinations. Estimate of sea level at time of growth determined on the basis of age, present-day elevation, and previously determined uplift rate of section (*40*, *62*, *64*). These sea-level ranges include uncertainties in uplift rate, age, and the water depth in which the coral lived. $\Delta\delta^{18}O$ values are the values determined for fossil corals compared with modern corals from the same locality on the Pee Dee Belemnite scale. ΔSST estimates were based on coral skeletal chemistry (*38*). The $\delta^{18}O$-based estimates include uncertainty in sea level. Values in parentheses indicate the source of the analyses from which the estimates are derived. *n*, number of analyses of successive monthly to two-monthly growth estimates. The presence of well-defined seasonality in each of the proxy records suggests minimal diagenetic disturbance. Nonetheless, each of the proxies for SST has some uncertainty associated with it, especially when applied to ancient corals. We conservatively assess these uncertainties to be up to ±2°C.

Coral and location; Huon Reef	Age (ka)	Estimated sea level (m)	$\Delta\delta^{18}O$ coral ($‰_{PDB}$)	Apparent ΔSST (source) (°C)
M93TBFC; Madang	**2.5 ± 0.4**	~0	+0.16	−0.8 ($\delta^{18}O$; *n*, 272)
Laing FC2	**2.7 ± 0.5**	~0	+0.14	−0.7 ($\delta^{18}O$; *n*, 583)
H95-16; I	**6.5 ± 0.07**	−1 to −13	+0.32	−0.9 **to −1.3** ($\delta^{18}O$; *n*, 564) +2.3 (Sr/Ca; *n*, 45)
H96-27; IIa	**38.3 ± 0.2**	−71 to −83	+1.13	−1.7 **to −2.3** ($\delta^{18}O$; *n*, 339)
H96-18; IIa	**39.4 ± 0.3**	−74 to −86	+1.20	−1.9 **to −2.5** ($\delta^{18}O$; *n*, 573) −2.4‡ (Sr/Ca; *n*, 53) −2.9 (Mg/Ca; *n*, 53) −1.7 (U/Ca; *n*, 53)
H96-36; IIa	38 to 40	−70 to −90	+1.19	−1.7 **to −2.6** ($\delta^{18}O$; *n*, 96)
H96-6; IIIb	**41.9 ± 0.1**	−52 to −64	+1.15	−2.7 **to −3.2** ($\delta^{18}O$; *n*, 27)
H97-10; V	~85	−24 to −44	+0.85	−2.1 **to −3.0** ($\delta^{18}O$; *n*, 153)
H95-14; VIa	**111.9 ± 0.6**	−45 to −66	+1.26	−3.1 **to −4.0** ($\delta^{18}O$; *n*, 318)
H94-2; VIIa (last interglacial)	118 to 128	~+5	+0.24	−1.4 ($\delta^{18}O$; *n*, 132) +1.0 (Sr/Ca; *n*, 111)
H95-58; VIIa (last interglacial)	118 to 128	~+5	−0.10	+0.2 ($\delta^{18}O$; *n*, 274)
H95-6; VII	130 ± 2*	−61 to −96	+1.13	−1.2 **to −2.7** ($\delta^{18}O$; *n*, 260)
H95-18; VII, Aladdin's Cave	130 ± 2†	−78 to −106	+1.81	−4.0 **to −5.2** ($\delta^{18}O$; *n*, 686) −5.9‡ (Sr/Ca; *n*, 152)§
H95-25; VII, Aladdin's Cave	130 ± 2†	−78 to −106	+2.04	−5.1 **to −6.0** ($\delta^{18}O$; *n*, 104)

*Coral H95-6 was collected from 12-m higher than Aladdin's Cave in the same section. Although this coral yielded ^{230}Th ages of ~125 to 126 ka [Web table 1 (*28*)], the $\Delta\delta^{18}O$ of this coral (implying much cooler SST and/or lower sea level), leads us to conclude that it also grew during the penultimate deglaciation, 130 ± 2 ka, possibly slightly after the corals in Aladdin's Cave. †Coral H95-18 was dated previously along with other corals from a location known as Aladdin's Cave. Although marginally acceptable [on the basis of $\delta^{234}U(T)$] ^{230}Th ages for this coral ranged from ~126 to 128 ka [Web table 1 (*28*)], dating of faviid corals from the same location, combined with stratigraphic, paleo-sea level, and paleo-SST considerations, indicate that this coral must have grown during the penultimate deglaciation, some time in the interval 128 to 132 ka (*54*, *64*). Coral H95-25 came from the same location, and has a similar $\Delta\delta^{18}O$. On these grounds, it is also assigned an age of 130 ± 2 ka. ‡Sr/Ca-based values which may overestimate cooling by 1° to 3°C due to proposed glacial-interglacial changes in oceanic Sr/Ca (*42*, *43*). §Previously reported Sr/Ca determinations (*54*).

with attendant increases in trade wind strength and thermocline slope (*32*–*34*). Tropic-equator (meridional) SST gradients may have been reduced at the LGM (*35*) [but see (*36*)], which would probably have been accompanied by weakened Hadley circulation (*37*).

The trace element and stable isotopic composition of the corals themselves can be used to infer mean climate conditions at the time of growth. Although each of the proxies for absolute SST estimation has uncertainties associated with it when applied to fossil corals, they can provide useful constraints. Our results (Table 1) (*38*) suggest that SST was similar to present around 2 to 3 ka, was 2 to 3°C cooler at 38 to 42 ka and ~85 ka, 3 to 4°C cooler at ~112 ka, similar to present at the last interglacial, and 2 to 6°C cooler during the penultimate deglaciation at 130 ± 2 ka. For the period around 6.5 ka, the $\delta^{18}O$ suggests similar or slightly cooler SST, whereas Sr/Ca suggest slightly warmer SST. This apparent discrepancy could reflect uncertainties in one or both proxy, or it may indicate that conditions were warmer but with decreased precipitation minus evaporation (i.e., drier) (*39*). These coral-based estimates of glacial SST are broadly in agreement with previous findings based on $\delta^{18}O$ of *Tridacna* clams from the Huon Peninsula (*40*) and with the deep-sea sediment data (*32*). The main exception is the extreme cooling (4° to 6°C) implied at ~130 ka by two corals (H95-18 and H95-25). However, if the salinity around Papua New Guinea were higher at this time [leading to less negative seawater $\delta^{18}O$, for example, due to decreased rainfall; but see (*41*, *32*)] and if oceanic Sr/Ca was increased (*42*, *43*) then the coral records could be interpreted as representing less extreme cooling.

Possible causes of changes in ENSO strength. Which aspects of the changes in climatic boundary conditions were responsible for the inferred changes in ENSO amplitude? It would appear that ENSO amplitude was not a simple function of the changing global temperatures (or sea levels) through the glacial-interglacial cycle (Fig. 5). Our records indicate that ENSO may have been weak around 6.5 ka, which is in agreement with inferences of subdued ENSO in the early- to mid-Holocene drawn from lake sediments in Ecuador (*44*), geoarchaeological evidence from Peru (*45*), and pollen data from Australia (*46*). However, ENSO was clearly operating during previous much colder "glacial" times around 38 to 42 ka and 130 ka and, possibly, during the early stages of the last deglaciation, 17.5 to 13.5 ka (*47*).

Changes in the seasonal distribution of solar radiation consequent on the precession cycle of orbital forcing are known to exert a strong influence over tropical climates, and recent modeling studies have suggested that precession may play an important role in determining ENSO variability. This effect on ENSO could be either internal to the Pacific (*9*, *48*) or related to the impacts on tropical atmospheric circulation of changes in the strength of the Asian Monsoon system (*49*, *50*). Using the Zebiak-Cane–coupled ocean-atmosphere climate model, which was developed specifically for ENSO studies, and forcing it with variations in heating due to orbital variations (*51*), Clement and co-workers (*9*, *48*) found major, precessionally controlled changes in ENSO variability through the last glacial-interglacial cycle (Fig. 5, D and E). The proposed mechanism is related to the timing of perihelion. When perihelion is in the boreal late summer–early autumn, zonally asymmetric heating of the equatorial Pacific results in an increase in trade wind strength, which in turn mitigates against the development of El Niño events. This results in a reduction in the ENSO variance and mean climatic conditions that are La Niña–like. Partial support for the precessional forcing hypothesis comes from the weak or absent ENSO during the early- to mid-Holocene and the possible occurrence of ENSO in the early stages of the deglaciation (*47*). However, our coral results indicate a relatively weak ENSO during at least two periods, around 38 to 42 ka and 130 ka, when the model predictions indicated the likelihood of ENSO stronger than the present day (Fig. 5).

We suggest that it is possible to reconcile our results with the model predictions by including the potential effects of the broader glacial-interglacial time scale changes in climate. The Zebiak-Cane model considers only the tropical Pacific Ocean, and the orbitally forced model runs do not include any changes in atmospheric CO_2 or changes in climate

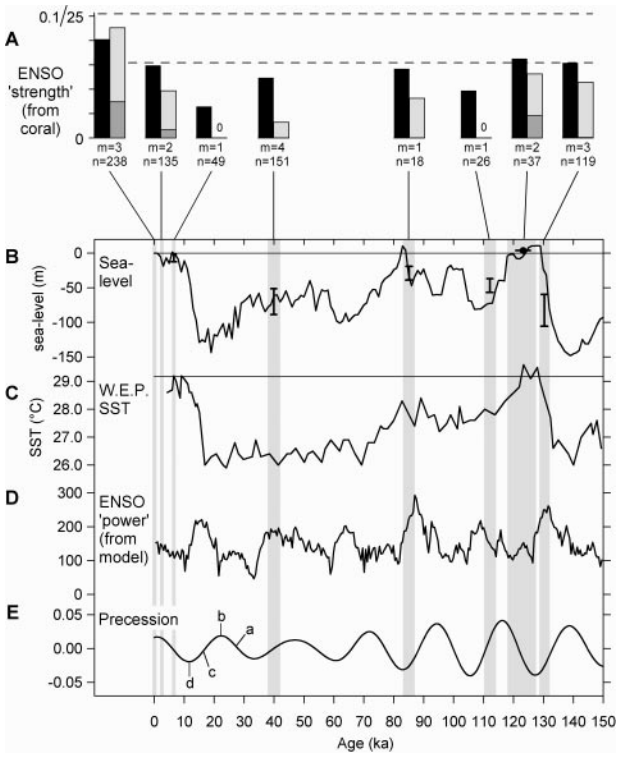

Fig. 5. (**A**) "Strength" of ENSO variability in coral $\delta^{18}O$ records for eight time periods over the past 150 ka. Solid black bars show the standard deviation (‰ units, on the 0 to 0.1 *y* axis scale) of the ENSO (2.5 to 7 year) bandpass-filtered coral $\delta^{18}O$ records from each time period. Shaded bars provide a measure of the occurrence of high-amplitude events for each period. The darker bars indicate the percentage of the data in the ENSO bandpass-filtered data that exceeds 0.15‰ absolute amplitude; lighter bars indicate the percentage of data that exceeds 0.10‰ amplitude (both plotted relative to the 0 to 25 scale on the *y* axis). *m*, number of corals combined for each group; *n*, total number of years represented by corals in each group. The horizontal dashed lines indicate the maximum and minimum standard deviation for sliding 30-year increments of modern coral $\delta^{18}O$ 2.5- to 7-year bandpass-filtered time series. (**B**) Estimate of global sea level (plotted as meters below present sea level) derived from benthic foraminiferal $\delta^{18}O$ (*61*). Bars indicate paleo–sea level estimated from the elevation, age, and uplift rate of corals analyzed in this study. These bars include uncertainty in the water depth in which the corals grew. Estimates of uplift rate are based on an assumed sea level of +5 m at 123 ka (circle and bar). (**C**) Sea surface temperature record for the western equatorial Pacific (ODP Hole 806B, 159°22′E, 0°19′N, 2520-m water depth) based on Mg/Ca composition of planktonic foraminiferans (*32*). The horizontal line indicates modern SST. (**D**) ENSO variability estimated from application of the Zebiak-Cane–coupled ocean-atmosphere model forced only by changing orbital parameters (*9*). Shown here is power in the 2- to 7-year (ENSO) band from multitaper spectral analysis of nonoverlapping 512-year segments of model NINO3 SST index. Power is approximately equal to 100× variance. Although there is considerable variation at sub-orbital wavelengths (2σ of power estimates ~±71 based on a control run with no change in orbital parameters), the main precessionally related features, including the trend of increasing ENSO amplitude and frequency through the Holocene, were found to be statistically significant (*9*, *48*). (**E**) The precessional component of orbital forcing (*51*). For one cycle, the timing of perihelion is indicated as follows: a, boreal autumn; b, boreal winter; c, boreal spring; d, boreal summer.

forced from outside the tropics. As a result, there is little change in the modeled mean temperature of the equatorial Pacific during glacial times, a scenario that now seems unlikely (*32*). We suggest that some aspect of the glacial climatic state may have had the effect of reducing the amplitude of ENSO. There are several possible candidates for this role. Significantly decreased equatorial Pacific temperatures may have resulted in generally weaker coupled ocean-atmosphere interactions, thereby subduing the ENSO system. Alternatively, or in addition to this, the inferred increase in zonal SST gradient in the equatorial Pacific may have subdued ENSO through strengthening of the trade winds. Although these are perhaps the most probable controlling factors, changed meridional SST gradients, tropical–extra-tropical interactions, and changes in thermocline structure (possibly related to any or all of the above) may also be implicated.

A dual control for ENSO consisting of a "glacial dampening" component and an orbital precession component would explain all the major features of our, and previously reported, paleo-ENSO data. The evolution from weak ENSO in the early- to mid-Holocene to strong and variable ENSO today was related to precessional effects (*9*, *48*). Moderate ENSO strength around 38 to 42 ka, 85 ka, and 130 ka was the net result of the competing effects of glacial dampening and precessional enhancement. Although we have only two short records from the last interglacial, they suggest similar or possibly slightly weaker ENSO than at present, in agreement with conclusions based on a coral record from Indonesia (*52*) and again consistent with our hypothesis. Lastly, our short record from 112 ka indicates relatively weak ENSO as might be expected with neutral precession effects (compared with present) and strong glacial dampening.

Our results, and our conclusions concerning a likely dual "orbital precession–glacial dampening" control mechanism over ENSO strength, lead us to suggest that ENSO may be stronger now than at any other time over the past 150,000 years. However, these data are sparse and need to be supplemented by adding high-resolution proxy records of ENSO from other locations and time periods before it will be possible to attribute the sensitivity of ENSO to specific aspects of global change. Such attribution is a prerequisite for successfully predicting the consequences of future greenhouse gas–induced warming on ENSO.

References and Notes

1. J. Bjerknes, *Mon. Weather Rev.* **97**, 163 (1969).
2. E. Rasmusson, T. Carpenter, *Mon. Weather Rev.* **110**, 354 (1982).
3. C. F. Ropelewski, M. S. Halpert, *Mon. Weather Rev.* **114**, 2352 (1987).
4. K. E. Trenberth *et al.*, *J. Geophys. Res.* **103 C7**, 14291 (1998).
5. N. E. Graham, *Clim. Dyn.* **10**, 135 (1994).
6. D. Gu, S. G. H. Philander, *Science* **275**, 805 (1997).
7. Y. Zhang, J. M. Wallace, D. S. Battisti, *J. Clim.* **10**, 1004 (1997).
8. M. A. Cane, *Science* **282**, 59 (1998).
9. A. C. Clement, R. Seager, M. A. Cane, *Paleoceanography* **14**, 441 (1999).
10. S. G. H. Philander, *El Niño, La Niña and the Southern Oscillation* (Academic Press, San Diego, CA, 1990).
11. J. D. Neelin *et al.*, *J. Geophys. Res.* **103 C7**, 14261 (1998).
12. A. Timmermann *et al.*, *Nature* **398**, 694 (1999).
13. T. R. Knutson, S. Manabe, D. Gu, D., *J. Clim.* **10**, 138 (1997).
14. M. Collins, *J. Clim.* **13**, 1299 (2000).
15. M. Latif *et al.*, *J. Geophys. Res.* **103 C7**, 14375 (1998).
16. F. E. Urban, J. E. Cole, J. T. Overpeck, *Nature* **407**, 989 (2000).
17. M. N. Evans, R. G. Fairbanks, J. L. Rubenstone, *Nature* **394**, 732 (1998).
18. A. W. Tudhope *et al.*, *Earth Planet. Sci. Lett.* **136**, 575 (1995).
19. S. Epstein, R. Buchsbaum, H. A. Lowenstam, H. C. Urey, *Bull. Geol. Soc. Am.* **64**, 1315 (1953).
20. J. J. Leder, P. K. Swart, A. M. Szmant, R. E. Dodge, *Geochim. Cosmochim. Acta* **60**, 2857 (1996).
21. Cores were collected vertically down the axis of maximum growth of corals whose upper surfaces were 3 to 4 m below mean low water spring (MLWS). tide level. Subsampling was achieved by milling with a slow-speed drill. Subsamples of 0.5- to 1.0-mg weight were analyzed for $\delta^{18}O$ and $\delta^{13}C$ on an isotope ratio mass spectrometer with automatic carbonate preparation system. Long-term analytical precision as determined by analysis of internal consistency standards is $\pm$0.16‰ $\delta^{18}O$ (2σ).
22. Throughout this paper, a bandwidth of 2.5 to 7 years [from application of a Gaussian bandpass filter (*53*)] has been used to characterize ENSO variability. However, during data analysis, we explored a variety of different filter widths, ranging from 2 to 8 years to 2.8 to 5 years. We also used spectral, cross-spectral, and evolutionary spectral analyses to investigate variability in the frequency domain. The results of these additional forms of time series analysis all lead to similar conclusions regarding changes in ENSO variability through time. That is, our conclusions are not sensitive to the precise definition of ENSO bandwidth nor on the form of time series analysis used.
23. J. Chappell, *Bull. Geol. Soc. Am.* **85**, 553 (1974).
24. _____, H. Polach, *Nature* **349**, 147 (1991).
25. M. Bar-Matthews, G. J. Wasserburg, J. H. Chen, *Geochim. Cosmochim. Acta* **57**, 257 (1993).
26. X-ray diffraction, petrographic thin-section, and scanning electron microscope (SEM) analyses were used to identify (and thereby reject for further study) corals that had experienced significant post-depositional alteration through cementation (in the marine or freshwater settings) or any recrystallization to calcite. This procedure was effective in screening corals for use of $\delta^{18}O$ as a climate proxy. For example, $>\sim$3% diagenetic calcite is required to make an analytically detectable (i.e., $>\sim$0.1 ‰) difference to the mean skeletal $\delta^{18}O$ value of these coral samples. However, trace elements in the coral skeleton may be more sensitive to subtle diagenetic alteration.
27. Analyses were obtained from combined thermal ionization mass spectrometry (TIMS) and alpha counting. Procedural blanks for ^{238}U are $<$1 pg and for ^{234}U $\sim 10^4$ smaller. Error in ^{232}Th is dominated by the uncertainty in the ^{232}Th blank correction (5 $\pm$ 2 pg) with blank for ^{230}Th being $\sim 10^4$ smaller. Ages are calculated using the relations as follows: $\delta^{234}U = \{[(^{234}U/^{238}U)/(^{234}U/^{238}U)_{eq}] - 1\} \times 10^3$. $(^{234}U/^{238}U)_{eq}$ is the atomic ratio at secular equilibrium and is equal to $\lambda_{238}/\lambda_{234} = 5.472 \times 10^{-5}$, where λ_{238} and λ_{234} are the decay constants for ^{238}U and ^{234}U, respectively. $\delta^{234}U(0)$ is the measured value; the initial value is given by $\delta^{234}U(T) = \delta^{234}U(0)e^{\lambda_{234}T}$, where T is the age in years. $(^{230}Th/^{238}U)_{act} = (^{230}Th/^{238}U)/(\lambda_{238}/\lambda_{230})$. ^{230}Th-ages are calculated iteratively using

$$1 - \left[\frac{^{230}Th}{^{238}U}\right]_{act} = e^{-\lambda_{230}T} - \left(\frac{\delta^{234}U(0)}{1000}\right) \times \left(\frac{\lambda_{230}}{\lambda_{230} - \lambda_{234}}\right)(1 - e^{(\lambda_{234}-\lambda_{230})T})$$

where T is the age in years and λ_{230} is the decay constant for ^{230}Th. $\lambda_{238} = 1.55125 \times 10^{-10}$ year^{-1}; $\lambda_{234} = 2.835 \times 10^{-6}$ year^{-1}; $\lambda_{230} = 9.195 \times 10^{-6}$ year^{-1}. The $2\sigma_M$ uncertainty in the age is determined by propagating the $2\sigma_M$ analytical contribution from the parameters $\delta^{234}U(0)$ and $(^{230}Th/^{238}U)_{act}$.
28. Web fig. 1 and Web tables 1 and 2 are available at *Science* Online at www.sciencemag.org/cgi/content/full/1057969/DC1.
29. A. W. Tudhope *et al.*, data not shown.
30. W. J. Conover, *Practical Nonparametric Statistics* (Wiley, New York, ed. 3, 1999), pp. 300–302.
31. The approximate null distribution of the Conover test is the standard normal distribution. Because the bandpass filter used here is centered roughly on 4.8 years, only the interannual peaks (maxima) and troughs (minima) associated with these pseudo-observations of ENSO variability contribute useful information on changes in ENSO amplitude. Therefore, we restricted our equality-of-variance tests to these interannual maxima and minima. This decision reduced the number of values used in the Conover test to roughly 12% of the original number of bandpass-filtered seasonal values. This large downward adjustment in the number of values (degrees of freedom) used in the tests still does not take into account the full effect of the bandpass filter on the independence of observations that the Conover test assumes for its null distribution. Therefore, we only consider as "significant" those differences in variance that exceed the nominal 99% significance level and warn against overinterpretation of the exact probability values [Web table 2 (*28*)].
32. D. W. Lea, D. K. Pak, H. J. Spero, *Science* **289**, 1719 (2000).
33. A. C. Mix, A. E. Morey, N. G. Pisias, S. W. Hostetler, *Paleoceanography* **14**, 350 (1999).
34. D. J. Andreasen, A. C. Ravelo, *Paleoceanography* **12**, 395 (1997).
35. CLIMAP Project Members, *Geol. Soc. Am. Map Chart Ser.* **36** (1981).
36. K. Lee, N. C. Slowey, *Nature* **397**, 512 (1999).
37. D. Rind, *J. Geophys. Res.* **103**, 5943 (1998).
38. Paleo-SST estimation from coral chemistry was achieved through comparison of data from living and fossil corals from our study sites on north coast Papua New Guinea using a temperature dependence relation of –0.21‰/°C for coral $\delta^{18}O$ (*19*, *20*) and previously published estimates of temperature dependence for Sr/Ca (*54*), Mg/Ca (*55*), and U/Ca (*56*). $\delta^{18}O$-based estimates assume 1.1‰ increase in mean ocean $\delta^{18}O$ for a 120-m drop in sea level (*57*) and zero net hydrological influence in the western equatorial Pacific (but see main text). Sr/Ca determinations (with the exception of H96-18; see below) were by TIMS; 2σ analytical uncertainty is better than 0.32% Sr/Ca. Mg/Ca, U/Ca, and Sr/Ca of H96-18 were determined by inductively coupled plasma–mass spectrometry (ICP-MS) using a combined internal standard-isotope dilution technique; 2σ analytical uncertainties are 0.7% in Sr/Ca, 1.8% in Mg/Ca, and 2.7% in U/Ca. Sr/Ca, Mg/Ca, and U/Ca ratios in fossil coral skeletons can be affected by diagenesis, even in samples where there is no evidence of cementation or recrystallization. Therefore, for these SST proxies we used the presence of well-defined seasonality in the trace element records that correlated with the $\delta^{18}O$ records from the same samples as the criterion for identification of unaltered cores. Data from corals that did not meet this criterion were rejected and are not presented here.
39. M. K. Gagan *et al.*, *Science* **279**, 1014 (1998).
40. P. Aharon, J. Chappell, *Palaeogeogr. Palaeoclimatol. Palaeoecol.* **56**, 337 (1986).
41. W. S. Broecker, *Paleoceanography* **4**, 207 (1989).
42. H. M. Stoll, D. P. Schrag, *Geochim. Cosmochim. Acta* **62**, 1107 (1998).

43. P. A. Martin, D. W. Lea, T. A. Mashiotta, T. Papenfuss, M. Sarnthein, *Geochem. Geophys. Geosyst.* [online] **1**, paper number 1999GC000006 (1999). Available at: http://g-cubed.org
44. D. T. Rodbell *et al.*, *Science* **283**, 516 (1999).
45. D. H. Sandweiss, J. B. Richardson III, E. J. Reitz, H. B. Rollins, K. A. Maasch, *Science* **273**, 1531 (1996).
46. J. Shulmeister, B. Lees, *Holocene* **5**, 10 (1995).
47. T. M. Rittenour, J. Brigham-Grette, M. E. Mann, *Science* **288**, 1039 (2000).
48. A. C. Clement, R. Seager, M. A. Cane, *Paleoceanography* **15**, 731 (2000).
49. Z. Liu, J. Kutzbach, L. Wu, *Geophys. Res. Lett.* **27**, 2265 (2000).
50. B. L. Otto-Bliesner, *Geophys. Res. Lett.* **26**, 87 (1999).
51. A. Berger, *J. Atmos. Sci.* **35**, 2362 (1978).
52. K. A. Hughen, D. P. Schrag, S. B. Jacobsen, *Geophys. Res. Lett.* **26**, 3129 (1999).
53. D. Paillard, L. Labeyrie, P. Yiou, *EOS* **77**, 379 (1996).
54. M. T. McCulloch *et al.*, *Science* **283**, 202 (1999).
55. T. Mitsuguchi, E. Matsumoto, O. Abe, T. Uchida, P. Isdale, *Science* **274**, 961 (1996).
56. G. T. Shen, R. B. Dunbar, *Geochim. Cosmochim. Acta* **59**, 2009 (1995).
57. D. P. Schrag, G. Hampt, D. W. Murray, *Science* **272**, 1930 (1996).
58. R. W. Reynolds, T. M. Smith, *J. Clim.* **7**, 929 (1994).
59. N. A. Rayner, E. B. Horton, D. E. Parker, C. K. Folland, R. B. Hackett, *Version 2.2 of the Global Sea-Ice and Sea Surface Temperature Data Set 1903–1994*, *Climate Research Technical Note 74* (Hadley Centre for Climate Prediction and Research, Bracknell, UK, 1996).
60. A. Kaplan *et al.*, *J. Geophys. Res.* **103 C9**, 18567 (1998).
61. N. J. Shackleton, *Science* **289**, 1897 (2000).
62. J. Chappell *et al.*, *Earth Planet. Sci. Lett.* **141**, 227 (1996).
63. J. Chappell, N. J. Shackleton, *Nature* **324**, 137 (1986).
64. T. M. Esat, M. T. McCulloch, J. Chappell, B. Pillans, A. Omura, *Science* **283**, 197 (1999).

65. We thank A. Clement for providing the data for Fig. 5D and for comments on an earlier draft of the manuscript, M. Cane and M. Mann for discussion on statistical analysis, and G. Mortimer for help in chemical procedures. Lamont-Doherty Publication no. 6140. Supported by UK Natural Environment Research Council grant GR3/09961.

1 December 2000; accepted 11 January 2001
Published online 25 January 2001;
10.1126/science.1057969
Include this information when citing this paper.

REPORTS

Observation of $d_{x^2-y^2}$–Like Superconducting Gap in an Electron-Doped High-Temperature Superconductor

T. Sato,[1] T. Kamiyama,[1] T. Takahashi,[1]* K. Kurahashi,[1] K. Yamada[2]

High-resolution angle-resolved photoemission spectroscopy of the electron-doped high-temperature superconductor $Nd_{2-x}Ce_xCuO_4$ (x = 0.15, transition temperature T_c = 22 K) has found the quasiparticle signature as well as the anisotropic $d_{x^2-y^2}$–like superconducting gap. The spectral line shape at the superconducting state shows a strong anisotropic nature of the many-body interaction. The result suggests that the electron-hole symmetry is present in the high-temperature superconductors.

The symmetry of the superconducting gap is directly related to the origin of superconductivity (*1*). For the hole-doped high-temperature superconductors (HTSCs), such as $La_{2-x}Sr_xCuO_4$ (LSCO), $YBa_2Cu_3O_7$ (YBCO), and $Bi_2Sr_2CaCu_2O_8$ (BSCCO), the general consensus is that they have an anisotropic $d_{x^2-y^2}$–like superconducting gap. But measurements from tunneling spectroscopy and magnetic penetration depth (*2*–*4*) experiments suggest that the electron-doped HTSCs such as $Pr_{2-x}Ce_xCuO_4$ (PCCO) and $Nd_{2-x}Ce_xCuO_4$ (NCCO) may have a different superconducting order parameter, possibly *s*-wave. The electron-doped HTSCs also appear different from their hole-doped counterparts in many physical properties such as displaying a narrower doping range of the superconducting phase (*5*). The relatively low maximum T_c (~25 K) and the electrical and thermal properties, interpreted by the Fermi liquid–like T^2 dependence, favor an *s*-wave symmetry. Thus, it has been believed that the superconducting order parameter and, therefore, the origin of superconductivity mechanism may be different for the hole- and the electron-doped HTSCs. However, recent tunneling (*6*), scanning SQUID (superconducting quantum interference device) microscope (*7*), and magnetic-penetration-depth (*8*, *9*) experiments have raised a question on this scenario, suggesting a *d*-wave symmetry for both types, whereas some other experiments (*10*, *11*) support the distinct difference in the superconducting order parameter between the two "different" HTSCs. Angle-resolved photoemission spectroscopy (ARPES) is powerful experimental technique to study the momentum-resolved (*k*-resolved) electronic structure of a material and has made an important contribution in establishing the superconducting order parameter in the hole-doped HTSCs (*12*, *13*). In comparison to the hole-doped HTSCs, the application of ARPES to study electron-doped HTSCs has not been so advanced. This has been due to the insufficient energy resolution to resolve the superconducting gap, which is much smaller than those of the hole-doped HTSCs, and due to the difficulty in growing high-quality single crystals of electron-doped samples.

We report high-resolution ARPES data on a high quality $Nd_{2-x}Ce_xCuO_4$ (x = 0.15, T_c = 22 K) single crystal and show that the NCCO has an anisotropic superconducting gap well described by the $d_{x^2-y^2}$-wave (*14*). The result suggests that electron-hole symmetry holds in the HTSCs and that the basic framework of the superconducting mechanism is similar between the electron- and the hole-doped HTSCs.

Single crystals of $Nd_{2-x}Ce_xCuO_4$ (x = 0.15, T_c = 22 K) were grown by the traveling-solvent floating-zone method and annealed in flowing Ar gas at 950°C for 10 hours. The magnetic susceptibility measurement shows that T_c is 22 K with a width of 2 K. ARPES measurements were performed using a SCIENTA SES-200 spectrometer with a high-flux discharge lamp and a toroidal grating monochromator. The energy and angular (momentum) resolutions were set at 12 meV (full width at half maximum) and ±0.1° (±0.01 Å^{-1}), respectively. A clean, flat surface of samples was obtained by in situ cleaving under ultrahigh vacuum of 5×10^{-11} Torr. Samples were cooled down by using a liquid He flow cryostat, and the temperature of the sample was monitored by a silicon diode thermocouple embedded in the sample substrate. Because surface degradation was found to occur relatively quickly, all spectra were recorded at 10 K within 2 hours after cleaving (*15*), during which any sign of degradation or contamination of the sample surface was not observed. We have confirmed the reproducibility of data with several different cleaves and samples. The Fermi level (E_F) of sample was referenced to that of a gold film evaporated onto the sample substrate.

The representative valence-band ARPES

[1]Department of Physics, Tohoku University, Sendai 980-8578, Japan. [2]Institute for Chemical Research, Kyoto University, Uji 611-0011, Japan.

*To whom correspondence should be addressed. E-mail: t.takahashi@msp.phys.tohoku.ac.jp